

Preparation and optimization of photocatalytic polyacrylic acid/guar gum/TiO₂ hydrogels for absorption and removing of methylene blue under Visible and UV irradiation

Seyyed Masud Naserzade

University of Tehran

Mohsen Shahrousvand

University of Tehran

Jamshid Mohammadi-Rovshandeh (✉ roshandeh@ut.ac.ir)

University of Tehran

Hojjat Basati

University of Tehran

Research Article

Keywords: Polyacrylic acid (PAA), Guar gum (GG), Response surface methodology (RSM), Titanium dioxide (TiO₂), semi-interpenetrating polymer networks (semi-IPNs)

Posted Date: June 10th, 2022

DOI: <https://doi.org/10.21203/rs.3.rs-1735510/v1>

License: © ⓘ This work is licensed under a Creative Commons Attribution 4.0 International License.

[Read Full License](#)

27 **Abstract**

28 Optimized polyacrylic acid/guar gum/Titanium dioxide (PAA/GG/TiO₂) hydrogels were
29 fabricated according to Design-Expert software. The intermolecular structures of the hydrogels
30 and the presence of nanoparticles were examined by scanning electron microscopy (SEM), Fourier
31 transform infrared spectroscopy (FTIR), and X-ray diffraction (XRD). To achieve dye absorption
32 rate, kinetic models such as pseudo-first-order, pseudo-second-order, Elovich, and intraparticle
33 diffusion (Weber-Morris), had been investigated in visible light and UV radiation at an initial
34 concentration of MB 20 (ppm) for one day. Diagrams of absorption isotherms in visible light and
35 UV irradiation at 20-60 (ppm) concentrations were evaluated based on the models of Freundlich,
36 Langmuir (Hanes-Woolf), Temkin, and Dubinin-Radushkevich. The hydrogel containing
37 crosslinker (4 mol %), TiO₂ (5 wt %), guar gum (2 wt %), and into the alkaline medium (pH=8)
38 was selected as superlative optimal status. The sample was examined for mapping of x-ray energy
39 diffraction (EDS) according to different elements densities of various circumstances to show the
40 degradation or absorption of methylene blue. The results showed that the prepared hydrogels have
41 a good efficiency for removing cationic contaminants from the aqueous medium and this property
42 is intensified by UV radiation.

43

44 **Keywords:** Polyacrylic acid (PAA), Guar gum (GG), Response surface methodology (RSM),
45 Titanium dioxide (TiO₂), semi-interpenetrating polymer networks (semi-IPNs).

46

47

48

49

50

51

52

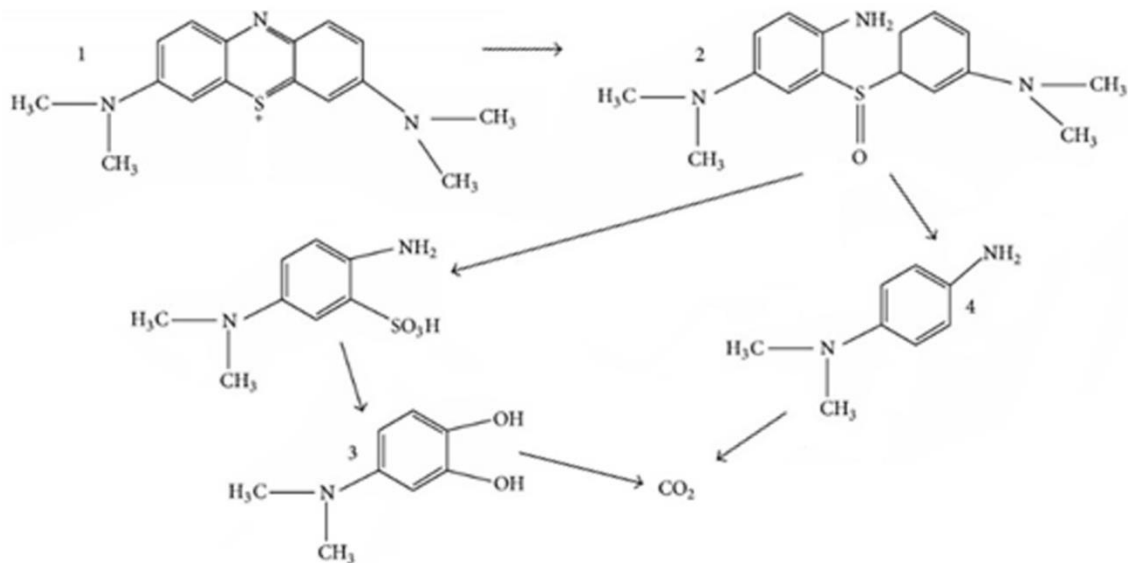
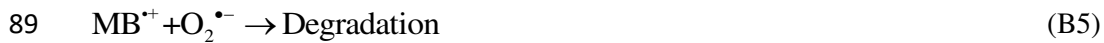
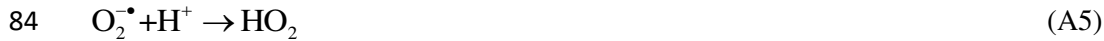
53

54 **1. Introduction**

55 The water crisis is one of the biggest challenges in the world. Water is polluted by hazardous
56 materials such as heavy oils, dyes, some heavy metals, etc [1-3]. Clean water resources are
57 dwindling continuously; therefore, refinement of wastewater operation has become one of the most
58 significant issues for the environment and the industries. Textile Industries use yearly over 150000
59 tons of water which can enter over 150 tons of cationic dye wastewater into nature and damage
60 human and marine creatures [4]. The presence of dye in water not only causes pollution and
61 toxicity but also prevents the passage of sunlight and can reduce the photosynthesis of marine
62 plants. Ultimately, lack of oxygen in the water leads to the death of aquatic animals [5]. Therefore,
63 the presentation of a method for removing dye from wastewater is vital before entering into nature.
64 For the removal of dyes in wastewater several methods can be utilized as Membrane Filtration [6],
65 Coagulation/Flocculation [7], Advanced oxidation [8], Ozonation [9], Electrocoagulation [10],
66 Adsorption or Absorption of hydrogel [11], photocatalytic degradation [12], etc.

67 The photocatalytic method has one of the best performances for the degradation of cationic dye
68 from wastewater [13]. Effects of bismuth vanadate (BiVO₄) as a photocatalytic substance were
69 investigated for degradation of methylene blue (MB) under visible light irradiation with the
70 assistance of potassium peroxymonosulfate. However, with UV radiation, the efficiency of the MB
71 degradation process increases predictably [14]. Graphene oxide and titanium dioxide (TiO₂)
72 composites were prepared to improve the degradation of MB pigment in the textile industry
73 effluent [15]. The behavior of several different composites was investigated for the degradation of
74 MB under UV irradiation at pH 2-10. The mechanism of MB degradation was based on water and
75 TiO₂ radical reactions (A1-5) and MB radical reactions (B1-5) [16]. When the semiconductor and
76 photocatalytic material of TiO₂ dispersed in water is exposed to ultraviolet light; the electron
77 travels from the valence band (VB) layer to the conduction band (CB) layer, causing radical
78 reactions (A1-5). These persistent reactions degrade MB (B1-5). The degradation of MB under
79 ultraviolet radiation is illustrated in Scheme 1.





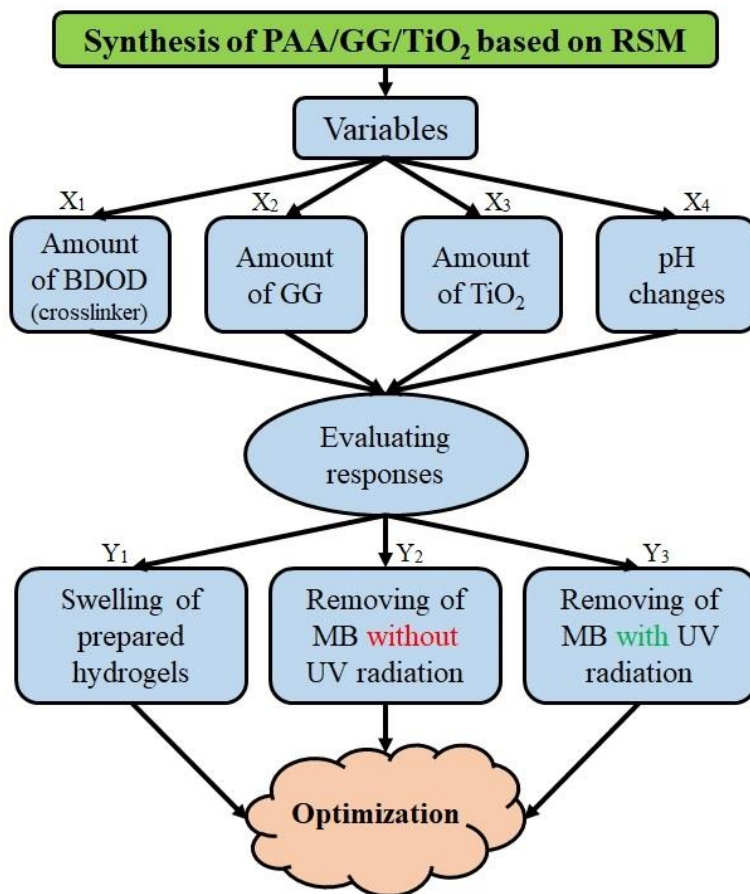
90

91 **Scheme 1.** Schematic of degradation of MB under UV radiation [16].

92 On the other hand, hydrogels as superabsorbent polymers (SAP) can increase the removal
 93 efficiency of contaminants. Therefore, superabsorbents containing photocatalytic materials can be
 94 prepared that are more efficient. For example, Mota et al. prepared Zn(II)-porphyrin/poly(acrylic
 95 acid) (Zn(II)Pr@PAA) microparticles as potential photocatalysts [17]. They suggested that the
 96 Zn(II)Pr@PAA microparticles are promise catalysts for photodegradation of aqueous organic
 97 pollutants in practical applications.

98 In this research, a creative method has been used to entrap and then ruin methylene blue.
 99 Photocatalytic semi-interpenetrating polymer network (semi-IPN) hydrogels based on PAA/Guar
 100 Gum (GG)/TiO₂ were prepared for the response surface methodology (RSM) application as shown
 101 in Scheme 2. MB absorption variable parameters such as amounts of gum, crosslinker,

102 nanoparticle, and pH were analyzed in visible light and under UV radiation and swelling ratio for
 103 optimizing RSM responses. Based on the optimization part of the RSM, the optimal samples and
 104 a control sample (without TiO₂) were synthesized, and XRD, FT-IR, and SEM analyses were
 105 performed to investigate the structure and presence of nanoparticles in the hydrogels. The
 106 absorption capacities of the optimal samples and control were obtained and compared. Kinetic and
 107 isotherm models of MB absorption were evaluated through the absorption capacity.



108
 109 **Scheme 2.** Algorithm for preparation and optimization of PAA/GG/TiO₂ nanocomposite
 110 hydrogels for MB removal.

111 2. Experimental

112 2.1. Material

113 Materials were used in this work include acrylic acid "AA" (Merck, Germany), distilled water,
 114 potassium persulfate "KPS" (Merck, Germany), titanium dioxide "TiO₂" (US Research
 115 Nanomaterials, TX USA), hydrochloric acid (Merck, Germany), Sodium hydroxide (Merck,

116 Germany), Methylene blue “MB” (Neutron, Iran), 1,4-Butanediol dimethacrylate ”BDOD”
117 (Merck, Germany), and Guar gum “GG” (Shanghai Macklin Biochemical Co., China).

118 **2.2. Synthesis method**

119 TiO₂ powder was dispersed into the distilled water. For TiO₂ uniformity, the TiO₂ mixture was put
120 into an ultrasonic device. The sample was irradiated in an ultrasonic cleaning bath (28 kHz, 1000
121 W) for 30 mins at room temperature. GG as a stabilizer was then added to the TiO₂ beaker and
122 stirred for 3 hrs. Then AA as a monomer, BDOD as a crosslinker, and KPS as an initiator were
123 then added into the beaker (based on experimental design). Eventually, the mixture was entered
124 into a silicon mold and cured in an oven at 100 °C for 30 minutes. After curation, the hydrogel was
125 settled into a beaker (more than 150 ml of distilled water) to separate unreacted monomers. Each
126 hydrogel was located in an oven at 50 °C for two days to dry and prepare for further evaluations.

127 **2.3. Experimental design**

128 The experimental design was drafted by Design-Expert program 11.0.3 from the central composite
129 design (CCD) subcategory of the response surface methodology (RSM) [18]. The amount of AA
130 was constant at 4g. Variables in the RSM were the quantities of BDOD (X₁), GG (X₂), TiO₂ (X₃),
131 and pH of absorption medium (X₄) which are noted in Table 1S and Scheme 2. Total runs
132 suggested by CCD can be obtained from Eq. (1).

$$133 \text{ Overall run numbers} = 2n+n^2+n_c \quad (1)$$

134 which n and n_c are the numbers of variables, and the central replicate runs, respectively. The
135 evaluating responses were swelling (Y₁), removing without UV radiation (Y₂), and removing with
136 UV radiation (Y₃). Also, one quadratic model was used for explaining the mathematical
137 relationship between the three independent variables by the following Eq. (2):

$$138 Y_j = b_0 + \sum_{i=1}^n b_i X_i + \sum_{i=1}^n b_{ii} X_{ii}^2 + \sum_{i=1}^{n-1} \sum_{j=i+1}^n b_{ij} X_i X_j \quad (2)$$

139 where, Y_j, b₀, b_i, b_{ii}, and b_{ij} are the predicted response, constant-coefficient, linear-coefficient,
140 quadratic equation, and interaction coefficient, respectively. In addition, X_i and X_j are the values
141 of variables. The CCD proposed 30 runs, as shown in Table 1. These samples were fabricated
142 based on what was described briefly.

143 **Table 1.** Central Composite experimental model with four independent variables and three
 144 responses

Run	X ₁	X ₂	X ₃	X ₄	Y ₁	Y ₂	Y ₃
1	8	1	5	6	382	93.1	96.9
2	6	1.5	10	7	429	93.1	96.1
3	6	1.5	0	7	413	90.5	95
4	8	2	15	6	183	92.3	97.6
5	6	1.5	10	9	326	95.8	97.8
6	4	2	5	6	410	93.6	98.9
7	8	2	5	8	383	94.9	96.9
8	4	1	5	6	525	93.1	97.7
9	10	1.5	10	7	325	92.5	98.7
10	8	2	15	8	318	95.9	99.2
11	6	1.5	10	7	429	93.1	95.9
12	6	1.5	10	7	429	93.1	95.9
13	8	1	5	8	383	94.6	96.4
14	6	2.5	10	7	305	92.2	97.2
15	6	1.5	10	5	385	89.1	95.3
16	4	2	5	8	455	96.9	98.8
17	4	1	15	6	299	88.3	94.9
18	6	1.5	10	7	429	93.1	95.7
19	2	1.5	10	7	500	89.1	94.4
20	6	1.5	20	7	277	89.1	93.2
21	4	2	15	8	432	95.9	98.7
22	4	2	15	6	185	88.2	93.6
23	6	1.5	10	7	429	93.1	95.7
24	6	1.5	10	7	429	93.1	95.7
25	8	1	15	6	378	90.1	93.2
26	4	1	15	8	389	92.6	96.9
27	4	1	5	8	595	92.3	94.8
28	8	1	15	8	347	94.2	96.4
29	8	2	5	6	385	90.4	94.5
30	6	0.5	10	7	582	88.7	89.6

145 **2.4. Swelling**

146 To determine the amount of swelling in the aquatic environment, as in previous studies [19, 20].

147 In summary, the chopped dry hydrogels were put into the distilled water. The surface water of
 148 hydrogels had been removed after 6 hrs in successive times and the weight of the samples was
 149 measured. The swelling ratio of samples was obtained by Eq. (3).

150 swelling percentage = $\frac{m_t - m_0}{m_0} * 100$ (3)

151 which m_0 is the weight of the dry hydrogel, and m_t is the weight of the swollen hydrogel at the
152 time (t).

153 **2.5. Absorption of MB in aqueous solution**

154 0.5 g prepared dry hydrogels were generally poured into the petri dish containing 50 ml of aqueous
155 MB pigment solution at a concentration of 20 ppm at different pHs for one day. In experiments,
156 the intensity of MB pigment was evaluated by UV-vis spectroscopy sequential times. The
157 percentages of absorption of MB were obtained by Eq. (4).

$$158 \text{ absorption percentage} = \frac{c_0 - c_t}{c_0} * 100 \quad (4)$$

159 which C_0 is the initial concentration of MB and C_t is the concentration of the solution after
160 absorption at the variable time (t).

161 **2.6. Characterization**

162 In this study, UV-vis spectroscopy model V-770 was used to measure the intensity of MB pigment
163 with an accuracy of 0.1 nm. Burker tensor 27 (made in Germany) FT-IR Spectrometer was used
164 to analyze the bond among the particles of the samples in the wavenumber of 400 to 4000 cm^{-1} .
165 SEM images using to observe particle size and the presence of TiO_2 nanoparticles in the hydrogel
166 using the AIS2100C device (made in South Korea). The amorphous or crystalline structure of the
167 hydrogels was examined and analyzed by an XRD device with a wavelength of X-ray lamp (1.5
168 angstroms), model PW1730 (manufactured by Philips, the Netherlands).

169 **2.7. UV chamber**

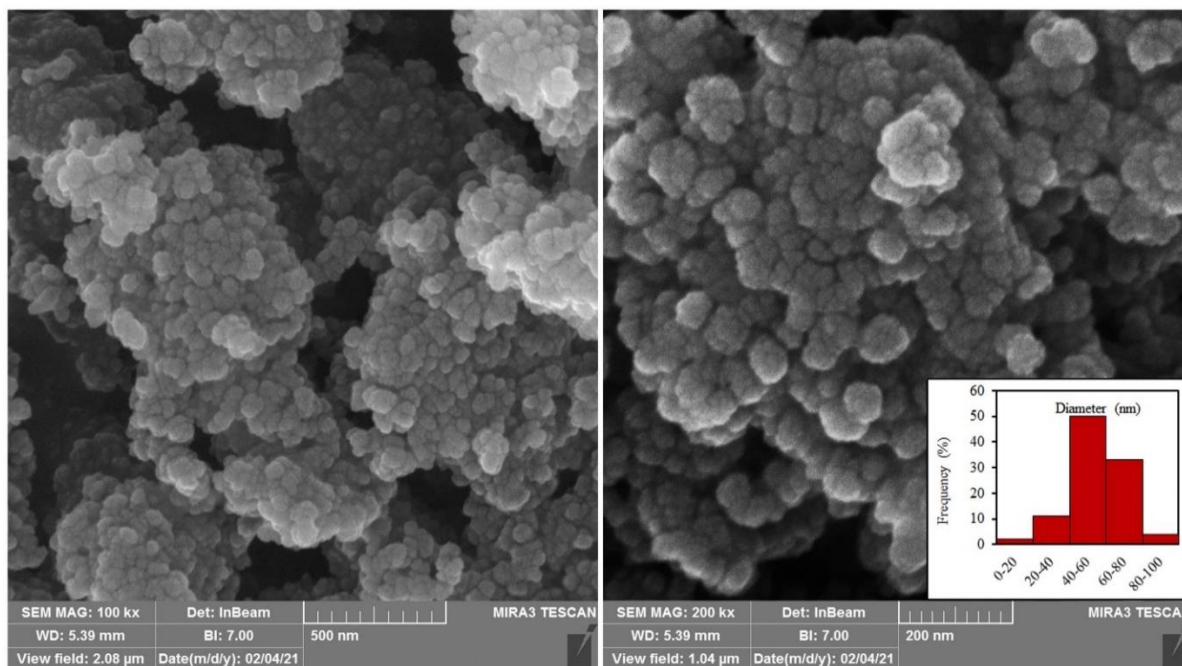
170 For the degradation of MB under UV radiation, a handmade UV chamber covered by aluminum
171 foil was designed. This device consists of the following parts such as a fan installed for air
172 conditioning, UV-C, and UV-AB lamps (Philips).

173 **3. Result and discussion**

174 **3.1. Synthesis of photocatalytic PAA/GG/ TiO_2 hydrogels**

175 Hydrogels were synthesized based on Table 1 and shown in Fig. 1S. As can be seen, all samples
176 were uniform. The samples containing TiO_2 nanoparticles were whiter and the dimensional
177 stability of the samples was improved by increasing the amount of crosslinking agent. For
178 example, run-3 was more transparent than the other samples. According to Table 1, some samples
179 contain different amounts of TiO_2 . For this purpose, from the TiO_2 used in this study, SEM images

180 and particle size distribution of TiO₂ were taken in Fig. 1. TiO₂ nanoparticles are spherical with
181 an average diameter of 60 nm.



182

183

Fig. 1. SEM images of TiO₂ particles at two magnifications.

184 3.2. Evaluation of hydrogel swelling as Y_1

185 The swelling rate of hydrogels as superabsorbents is a key parameter. The swelling of synthesized
186 hydrogels was evaluated and shown in Fig. 2. Run-8, run-19, run-27, and run-30, which had high
187 swelling rates, had a low cross-linking agent. Likewise, run-4 and run-22 have low swelling ratios,
188 which can be due to the higher amount of crosslinks. According to Table 1, run-22 had a
189 crosslinker of 4%, which was not the highest value. Therefore, it seems that the synergistic effect
190 of other variables has been involved challengingly. The analysis of software results is shown in
191 Fig. 2S. In contour diagrams, red and blue regions indicate the highest and lowest response values
192 respectively. Therefore, the color spectrum changes between blue and red. The swelling contour
193 diagrams are almost green, plus no drastic changes can be distinctive. The lower is the crosslinker,
194 the yellower would be the swelling ratio. The results confirm that increasing the amount of TiO₂
195 nanoparticles reduces the amount of swelling. Since these nanoparticles can prevent water from
196 entering their structure, they can swell by creating an interaction between the polymer chains. The
197 results show that the pH value in the alkaline range is optimal. Previous scholars proved that PAA
198 swells more in alkaline environments [21, 22].

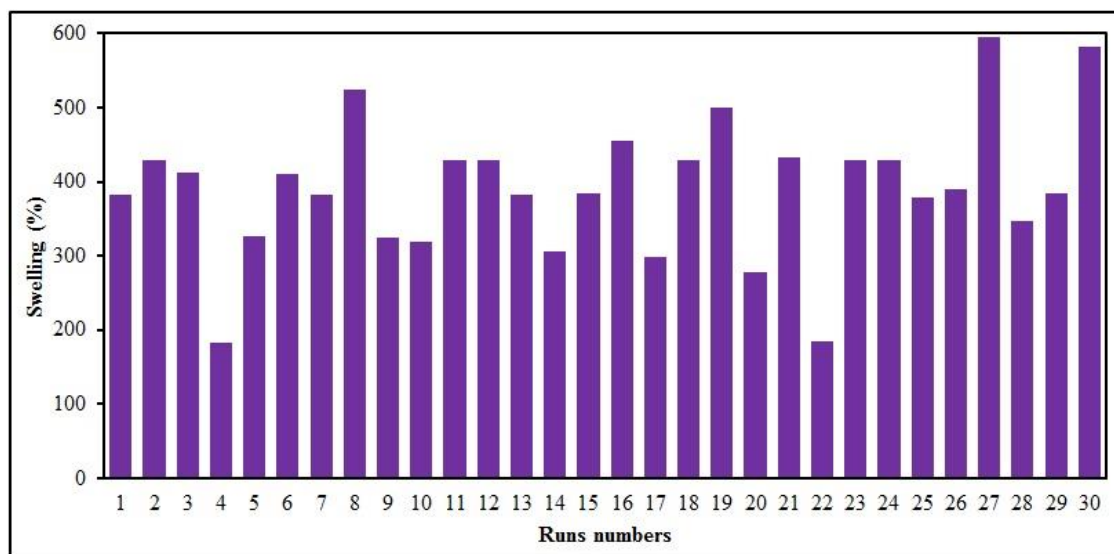
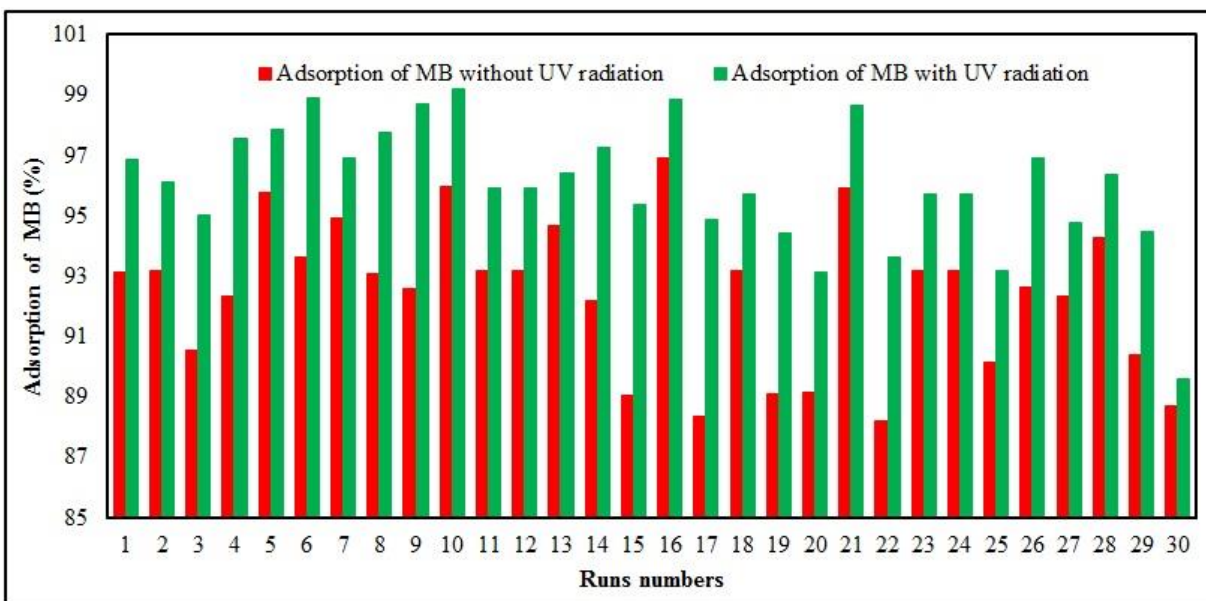


Fig. 2. Experimental evaluation of the swelling rate of the synthesized samples.

3.3. Evaluation of MB absorption in visible and UV light as Y_2 and Y_3

According to Fig. 3, all runs for absorption of MB in the UV chamber are significantly higher than absorption in visible light. The significant increase can also be due to TiO_2 photocatalytic nanoparticles. Other factors affect the absorption percentage in the two environments. Based on the contour diagrams of the methylene blue absorption in the visible light environment (Fig. 3S). The effect of the alkali environment on the absorption of MB cation dye is more favorable than in the acidic environment. Comparing the contour diagram in both visible and UV radiation environments (Fig. 3S and Fig. 4S), it is obvious that the yellow and red areas are more due to UV radiation. When the pH reaches 8, the color changes from green to yellow, and red emerges in the graphs; therefore, increasing the pH is the most effective factor in the absorption ratio of MB in visible light. Fig. 3S indicates that the percentage of absorption increases by scale-up the amount of GG from 1 to 2 (wt %) and reduction of BDOD from 8 to 4 (mol %). The most valuable point in the absorption diagram in Fig. 3S, increasing the amounts of TiO_2 and BDOD have a very adverse effect on the absorption of MB. Therefore, the minimum amount of these two factors have a favorable influence on improving the absorption of MB from the aqueous solution. With increasing pH, the absorption of MB pigment increases impressively, and the amount of BDOD has no absorption effect. Fig. 3S likewise mentions that the improvement of absorption ratio occurs by changing the amount of GG from 1 to 2 (wt %) and TiO_2 from 15 to 5 (wt %). Moreover, the

219 results indicate that with increasing the pH and the amount of GG, the absorption of MB pigment
220 from the aqueous solution increases drastically.

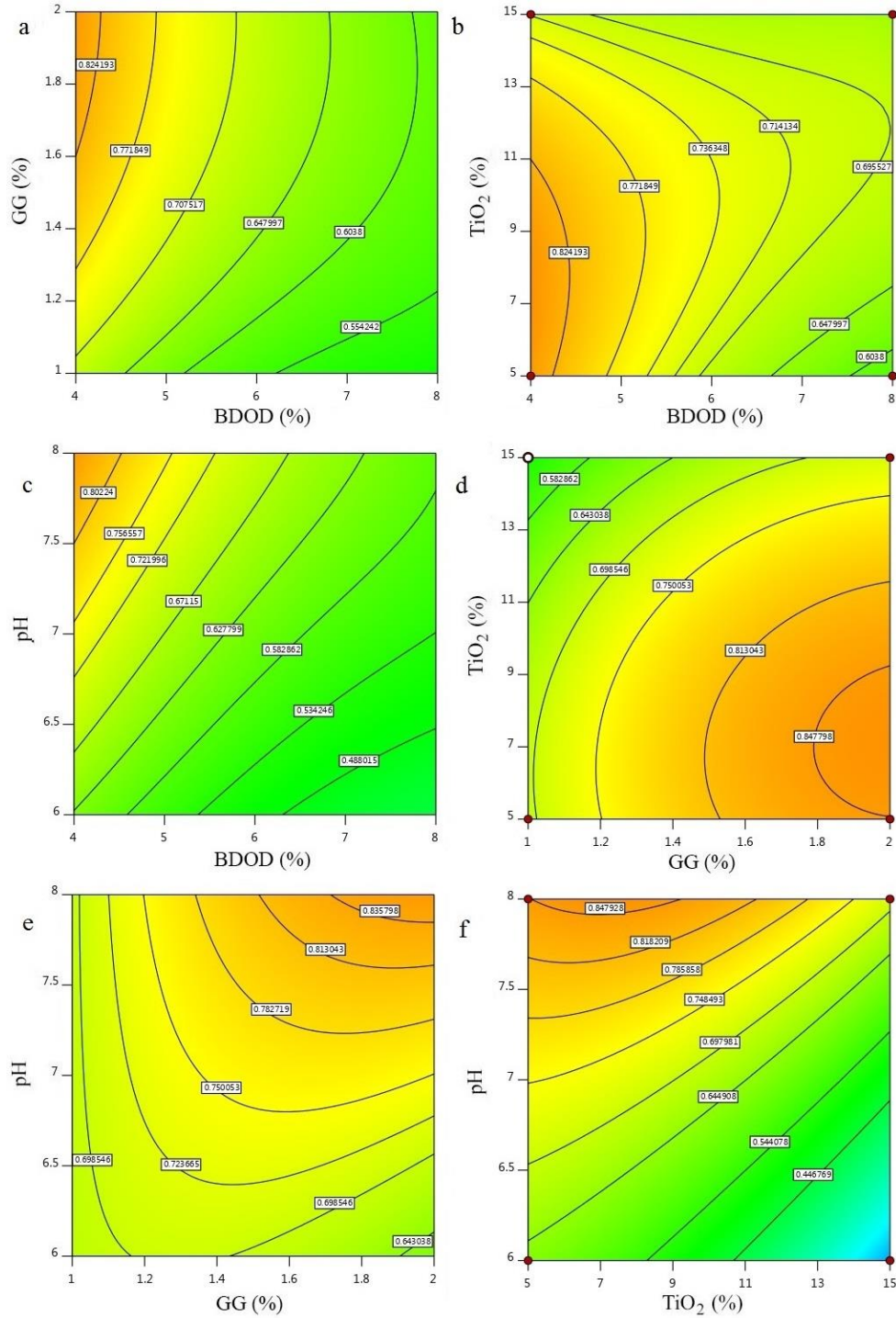


221
222 **Fig. 3.** Experimental evaluation of MB absorption with synthesized samples in both visible light
223 and UV radiation

224 As shown in Fig. 4S, yellow and red colors expose in most images, which manifests the efficiency
225 of MB absorption under UV radiation compared with visible light. According to the colors and
226 prior discussion, the best state of absorption is at pH = 8, but this graph can prove which demanded
227 absorption perform intensively at pH=6 under UV irradiation. The absorption process at pH=6 was
228 favorable because of the radical reactions of water by activating the photocatalytic properties of
229 TiO₂ nanoparticles, and the absorption status of TiO₂ 5-7 (wt %) and pH=8 is the foremost
230 circumstance of absorption of MB under UV light.

231 **3.4. Design expert results**

232 Base on Tables 2S, 3S, and 4S, all responses are significant. As shown in the color spectrum of
233 Fig. 4, when TiO₂ reaches 15 wt%, the graphs approach blue. When pH=8 and GG=2 (wt %); the
234 color spectrum tends to red regularly, so increasing the pH and GG have the most positive effect
235 on the desirability. BDOD (mol %) has the worst effect on the ratio of desirability. Thus, by
236 increasing BDOD from 4 to 5 mol% the amount of desirability in the response is declined crucially.
237 Distinctly, by dwindling the amount of TiO₂ to 9 (wt %), the ratio of desirability increases.



238

239

Fig. 4. Diagrams of the effect of different factors of design expert on the ratio of desirability.

240

After analyzing the swelling and absorption responses by the design expert program, in the

241

optimization segment, two optimal and control (no TiO₂) samples were proposed, specifications

242

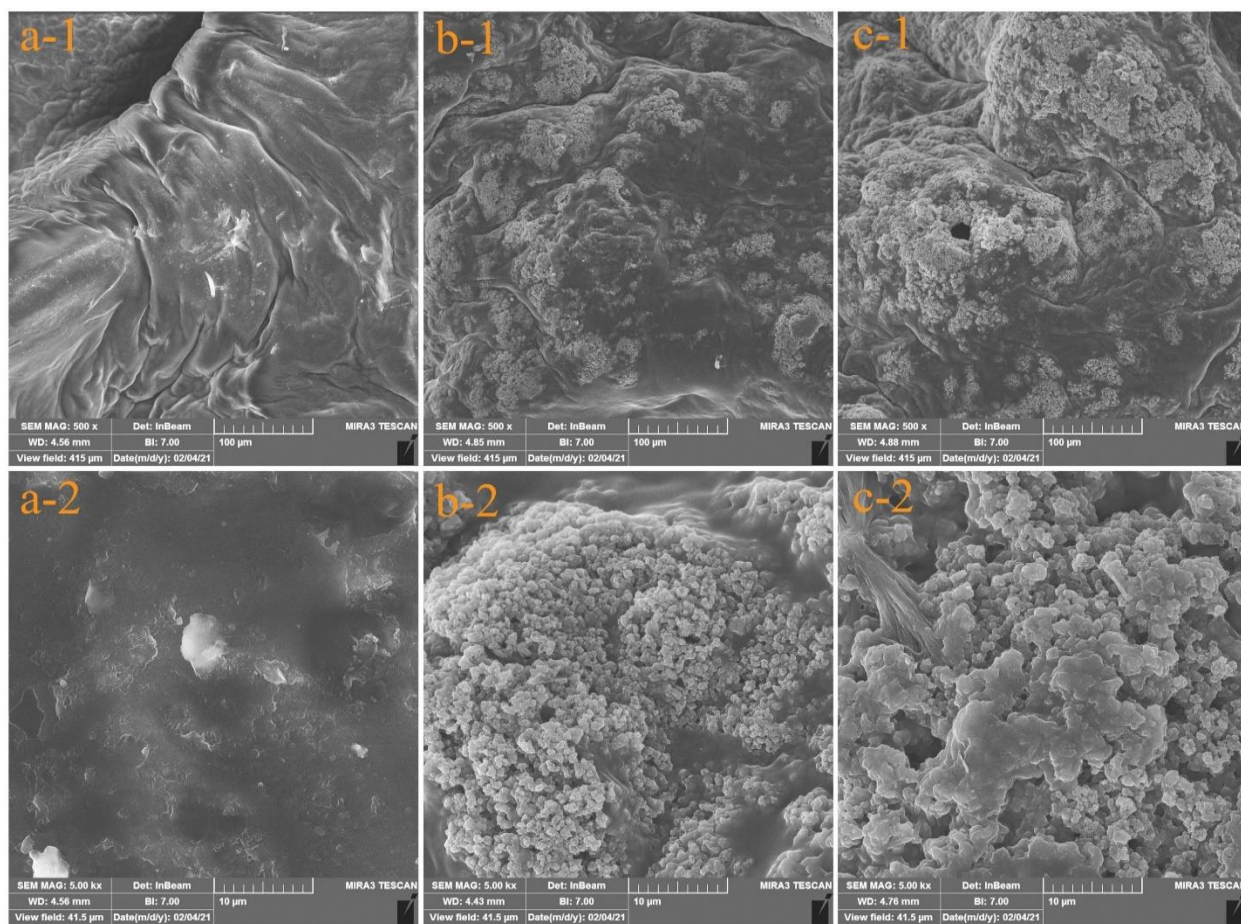
of these samples are evident in Table 2.

243 **Table 2.** Combining the percentage of materials of optimal and control samples

Name of samples	BDOD (mol %)	GG (wt %)	TiO ₂ (wt %)	pH
Control	4	2	0	8
Optimum-1	4	2	5	8
Optimum-2	4	2	7	8

244 **3.5. Morphological study of the fracture surface**

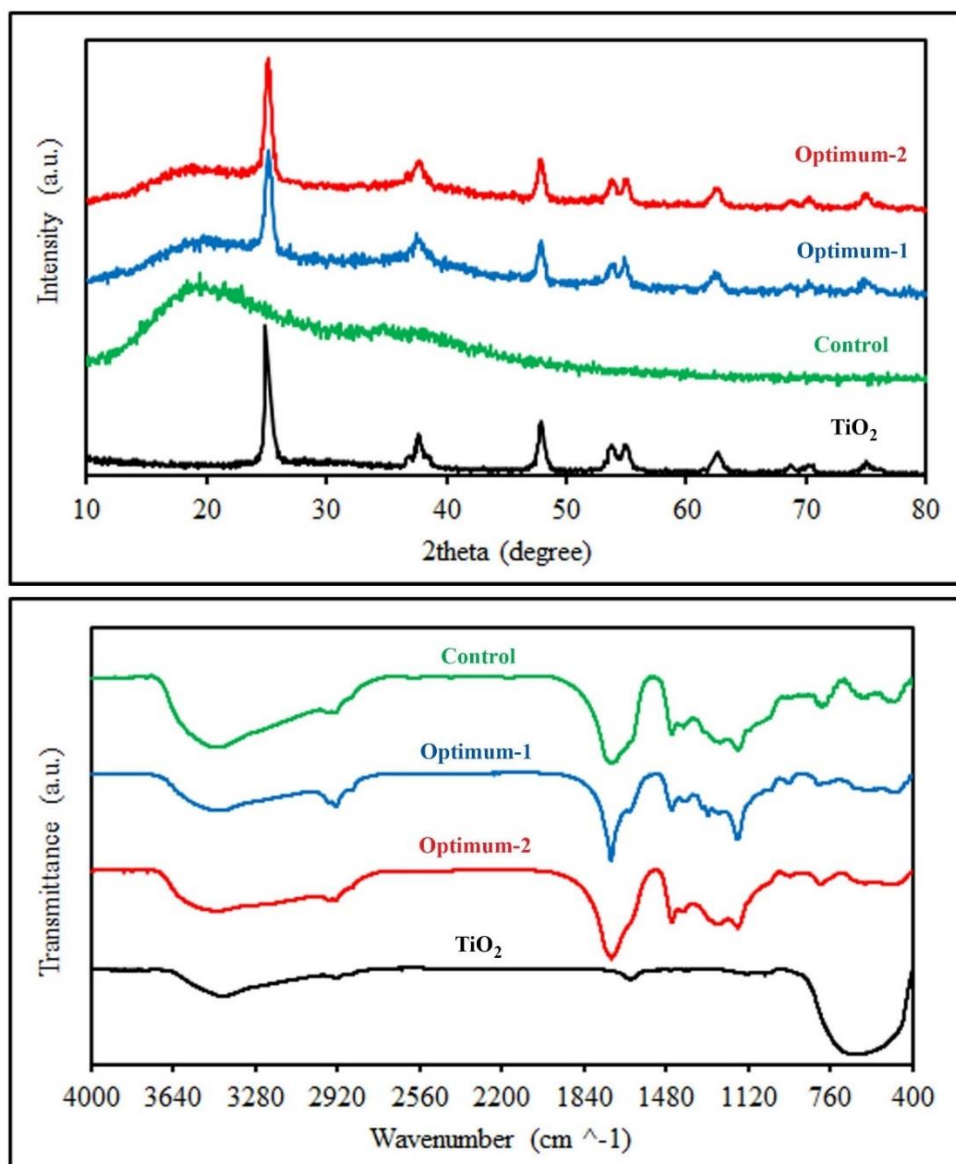
245 SEM images of the cross-section of the optimal samples and the control sample are shown in Fig.
 246 5. In Optimum-1 and Optimum-2, the presence of TiO₂ nanoparticles can be seen. These
 247 nanoparticles exhibit as lumps, in the optimal-2 is increased the intensity of aggregations
 248 excessively.



249 **Fig. 5.** SEM cross section images of (a-1 and a-2) control, (b-1 and b-2) optimum-1, and (c-1 and
 250 c-2) optimum-2 at two magnification.
 251

252 **3.6. XRD and FTIR analyses**

253 Standard XRD patterns are for optimal and control samples in the angle range $2\theta=10-80^\circ$. Since
254 no peak diffraction in the control sample diagram is apparent in Fig. 6 is amorphous. TiO_2
255 nanoparticles where they locate into the morphology of hydrogel; the morphology of the hydrogel
256 alternates from an amorphous status to the crystalline composites, and the peak angles of this
257 nanoparticle are constant in most of the hydrogels. Dispersions of TiO_2 nanoparticles are
258 contributed in Fig. 6a at angles of $2\theta=27^\circ, 38^\circ, 48^\circ, 54^\circ, 56^\circ, 63^\circ, 69^\circ$, and 71° [23].



259

260

Fig. 6. XRD and FT-IR analysis of control and optimal samples, and TiO_2

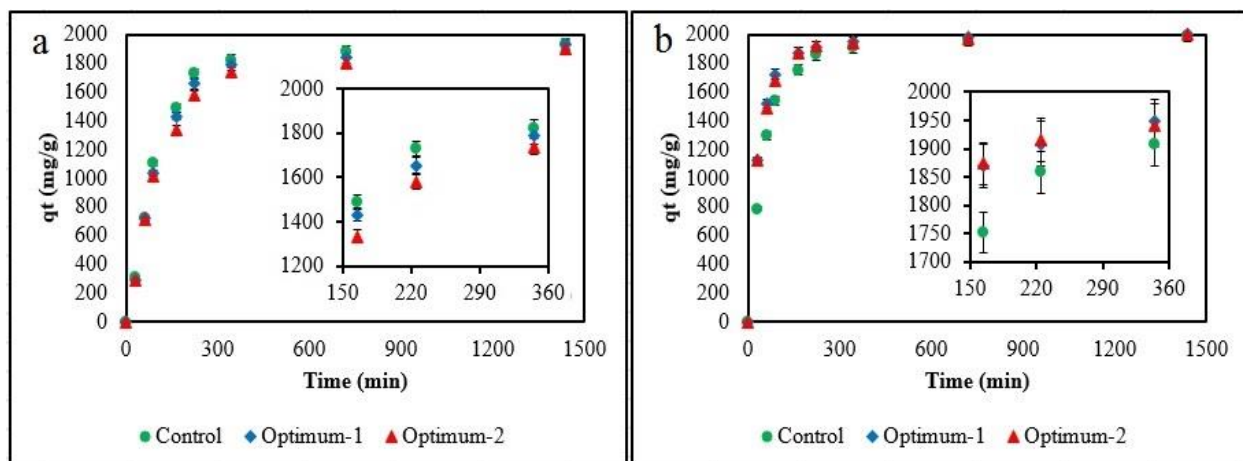
261 The intensity of peaks in Optimum-2 is higher than in Optimum-1, which indicates a higher amount
262 of TiO₂ nanoparticles. According to Fig. 6, the FTIR of the fabricated samples is definite in the
263 range of 400-4000 cm⁻¹. The peak at 3436 cm⁻¹ relates to the stretching bond of the hydroxyl
264 functional group due to intermolecular hydrogen bonding. At the climax point 2929 cm⁻¹, the
265 stretching bonds can attribute to the medium bonds of the alkane group. The wavenumber roughly
266 1718 cm⁻¹ should pertain to the tenacious stretching vibrations of the carbonyl group of polyacrylic
267 acid [24]. The wavenumbers 1454 and 1162 cm⁻¹ relates to the medium bending bonds of methyl
268 substations and the medium stretching bonds of the amine group, respectively. Between 900-500
269 cm⁻¹ wavenumber locating in the fingerprint zone; relates to the symmetric and asymmetric links
270 of Ti-O-Ti [25].

271 **3.7. Evaluation of MB absorption by optimal and control hydrogels**

272 The UV-vis spectroscopy reports the intensity of the colors (Abs) based on the index peaks. MB
273 dye has different peak places such as 300, 585, and 665 nm as is shown in Fig. 5S. The most
274 intense considering peak is 665 nm as the base peak to obtain the desired concentration. For this
275 aim, calibration curves at a variety of concentrations of MB were assessed. Volume capacity
276 depends on the volume of the solution (ml) and the initial concentration of C₀ and in a variable
277 time C_t (ppm) and the amount of absorbent W (g) if the volume (V) of the solution containing the
278 fixed pigment; Eq. (6) pertains to absorption capacity (q_t).

$$279 \quad q_t = V \frac{(C_0 - C_t)}{W} \quad (6)$$

280 The results of absorption capacity of MB by hydrogels over time are shown in Fig. 7. As it is
281 shown in Fig.7a, MB was absorbed by the control sample 1780 mg/g in 225 min, but Optimum-1
282 and Optimum-2 could have absorbed about 1600-1650 mg/g MB for 225 min at visible light
283 condition. Therefore, MB absorption rate is more in control than optimums at without UV
284 radiation. Fig 7b show the MB absorption by Optimum-1, Optimum-2, and control in the UV
285 chamber. The absorption capacity rate of the Optimum-1 is higher than all samples and is
286 approximately 1720 mg/g in 90 minutes. It is noteworthy that Optimum-2 has an equilibrium
287 absorption capacity of 1896 mg/g in visible light, but when it is placed under UV light, it increases
288 nearly 1996 mg/g after 1500 min, which can effectively infer the photocatalytic hydrogel activity
289 at UV chamber.



290
 291 **Fig. 7.** The absorption capacity of MB pigment by optimal and control samples a) in visible light
 292 b) under UV radiation

293 3.8. Kinetic absorption models

294 For obtaining the absorption pace and the rate-limiting step, several absorption kinetic models are
 295 used. The kinetic models of the pseudo-first-order Eq. (7), pseudo-second-order Eq. (8),
 296 intraparticle diffusion (Weber-Morris) Eq. (9), and Elovich Eq. (10) based on absorbent capacity:

$$297 \ln(q_e - q_t) = \ln q_e - k_1 t \quad (7)$$

$$298 \frac{t}{q_t} = \frac{1}{k_2 q_e^2} + \frac{t}{q_e} \quad (8)$$

$$299 q_t = k_d t^{1/2} + C \quad (9)$$

$$300 q_t = \frac{1}{\beta} \ln(\alpha\beta) + \frac{1}{\beta} \ln t \quad (10)$$

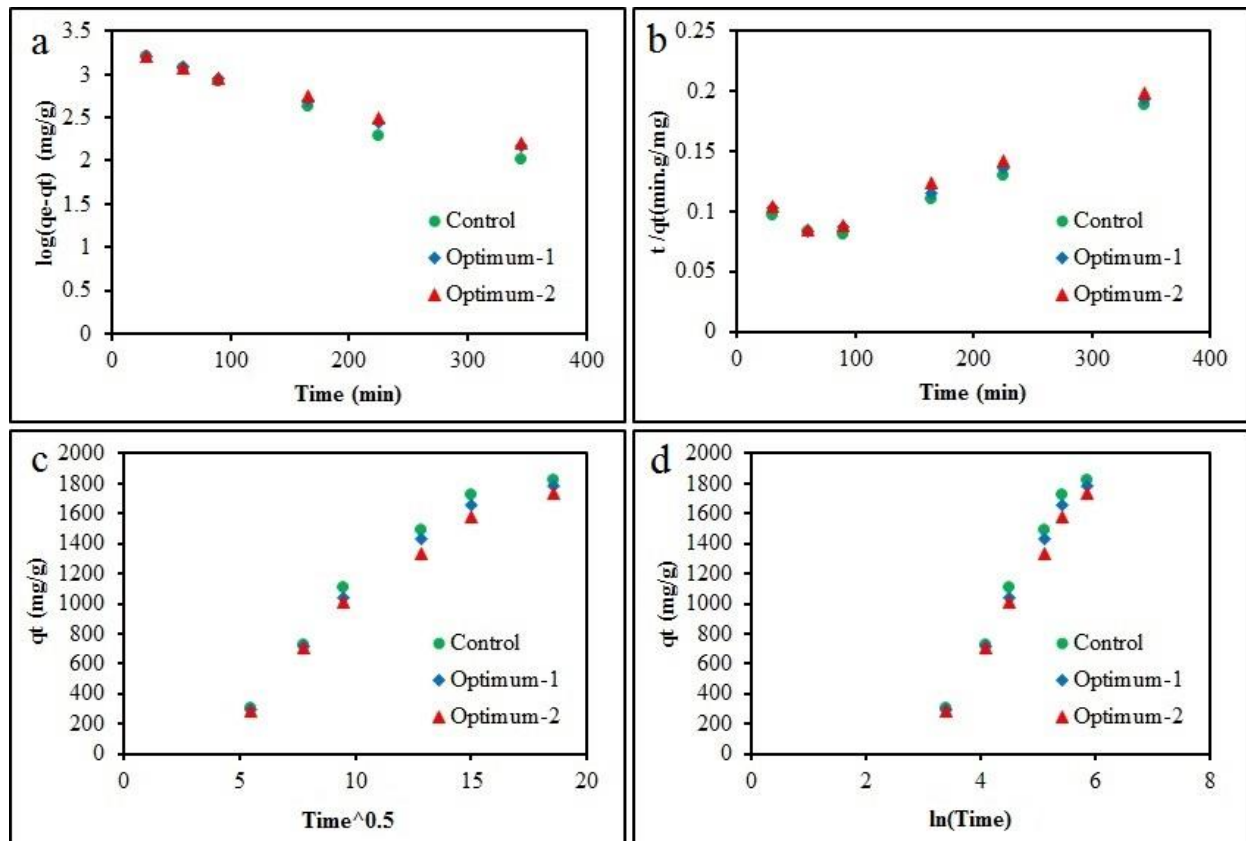
301 That χ is calculated by Eq. (11):

$$302 \chi^2 = \frac{(q_{(cal)} - q_{(exp)})^2}{q_{(exp)}} \quad (11)$$

303 In all kinetic Eq.s of this work, q_t and q_e are the quantities of pollutants absorbed at t (min) and
 304 equilibrium status, respectively. k_1 (min^{-1}) in Eq. (7) is the pseudo-first-order absorption rate
 305 constant, k_2 ($\text{g} \cdot \text{mg}^{-1} \cdot \text{min}^{-1}$) in Eq. (8) is the equilibrium constant of the pseudo-second-order; C is
 306 a constant of diffusion resistance (mg/g) and a constant rate of intraparticle diffusion, k_d ($\text{mg} \cdot \text{g}^{-1}$
 307 $\cdot \text{min}^{-0.5}$) in Eq. (9). Elovich's two constants are initial absorption rate α ($\text{mg} \cdot \text{g}^{-1} \cdot \text{min}^{-1}$) and
 308 desorption constant β (g/mg) in Eq. (10).

309 Fig. 8 and Table 3 show kinetic absorption model diagrams and constants in visible light. As it is
 310 shown, the kinetic model of Elovich absorption with an average of $R^2=0.99$ is a favorable kinetic

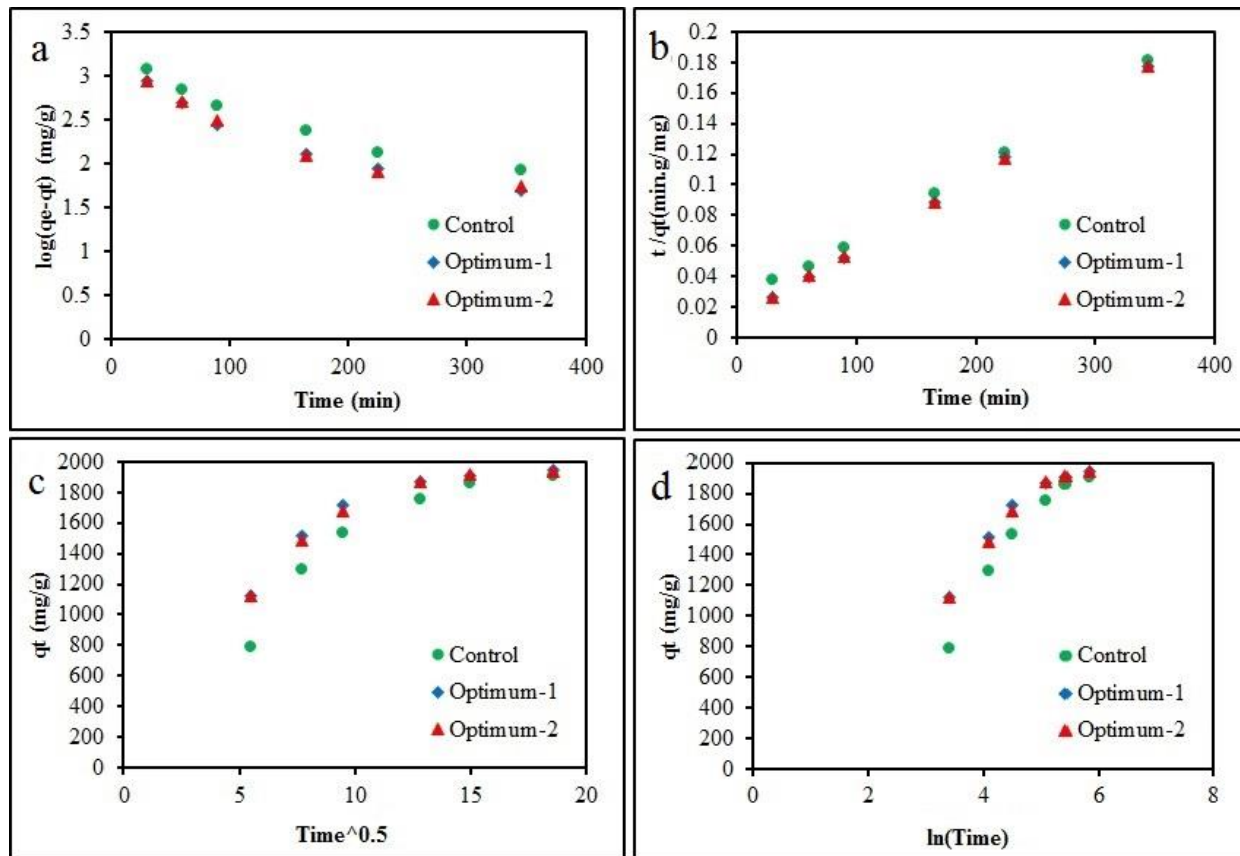
311 model for absorption in visible light. This is while the $q_e(\text{cal})$ corresponds better to the $q_e(\text{exp})$
 312 value by pseudo-first-order.



313
 314 **Fig. 8.** Diagrams of kinetic models, a) pseudo-first-order, b) pseudo-second-order, c)
 315 intraparticle diffusion, and d) Elovich in visible light

316 Due to the closeness of the mean $q_e(\text{cal})$ of the pseudo-first-order kinetic models of 1878 mg/g to
 317 the average of $q_e(\text{exp})=1910$ mg/g compared to the Elovich model with the average of
 318 $q_e(\text{cal})=2550$ mg/g. Therefore, with the help of one model alone, the result cannot be obtained and
 319 both the pseudo-first-order model and the Elovich model can be useful at the same time. As shown
 320 in Fig. 9 and Table 3, following the table can be found out these results: The pseudo-first-order
 321 model with averages of $R^2=0.92$ and $\chi^2=1495$ cannot be a preferable model for the absorption
 322 kinetics. Fig. 9b, the pseudo-second-order model with an average of $R^2=0.999$ and $\chi^2=0.011$ should
 323 report a perfect model for UV absorption kinetics. Fig. 9c, the intraparticle diffusion model cannot
 324 expose an acceptable for the UV absorption kinetic model and so on. Since the average of
 325 $q_e(\text{cal})=2000$ mg/g of the pseudo-second-order kinetic model is closer to the average of
 326 $q_e(\text{exp})=1995$ mg/g than other models, the pseudo-second-order model is the best model for

327 absorbing MB pigment in the UV chamber. Base on the Elovich model from the Table 3, the initial
 328 absorption rate MB under UV light is faster than visible light.



329
 330 **Fig. 9.** Diagrams of kinetic models, a) pseudo-first-order, b) pseudo-second-order, c)
 331 intraparticle diffusion, and d) Elovich under UV radiation

332
 333 **Table 3.** Evaluation of kinetic models of absorption in visible light and UV chamber

constants	Vis			UV		
$q_e(\text{exp})$	Control=1897	Optimum-2=1896	Optimum-1=1934	Control=1992	Optimum-2=1996	Optimum-1=1998
Pseudo-first-order model						
$q_e(\text{cal})$	1938	1830	1878	1112	786	769
k_1	0.00169	0.00139	0.00143	0.00829	0.00875	0.00875
χ^2	0.0937	2.437	1.712	666	1860	1959.4
R^2	0.9807	0.991	0.986	0.941	0.906	0.924
Pseudo-second-order model						
$q_e(\text{cal})$	3333	3333	3333	2000	2000	2000
$k_2(*10^6)$	1.363	1.264	1.283	12.6	22.7	23.8
χ^2	594	618	586	0.008	0.024	0.002
R^2	0.886	0.905	0.883	0.997	0.999	1
Elovich model						

$q_e(\text{cal})$	2867.02	2655.06	2776.81	2687.85	2538.48	2532.59
α	35.98	33.53	34.41	112.9	404.5	449.25
β	0.00152	0.00165	0.00156	0.0022	0.0029	0.003
χ^2	328.19	217.01	255.81	180.148	115.93	112.84
R^2	0.985	0.995	0.992	0.9404	0.928	0.913
Intraparticle diffusion model						
k_d	118.1	109.8	115.1	79.88	59.2	57.82
C	163.6	-154.5	-174.5	602	998	1014
R^2	0.927	0.949	0.941	0.833	0.814	0.792

334 **3.9. Isotherm absorption models**

335 The absorption isotherm is the relation between the absorbed pigment capacity and the different
336 pigment concentrations in an aqueous solution under equilibrium status based on initial
337 concentration of pigment. There are several equations for isotherm models, from which we can
338 refer to the Freundlich isotherm model of Eq. (12), the Langmuir (Hanes-Woolf) Eq. (13) [26],
339 and the Temkin Eq. (14), and the Dubinin-Radushkevich (D-R) Eq. (15).

$$340 \log(q_e) = \log(k_F) + \frac{1}{n} \log(C_e) \quad (12)$$

$$341 \frac{1}{q_e} = \frac{1}{q_m} + \frac{1}{k_L q_m C_e} \quad (13)$$

$$342 q_e = b_1 \ln(k_T) + b_1 \ln(C_e) \quad (14)$$

$$343 \ln(q_e) = \ln(q_m) - \beta \epsilon^2 \quad (15)$$

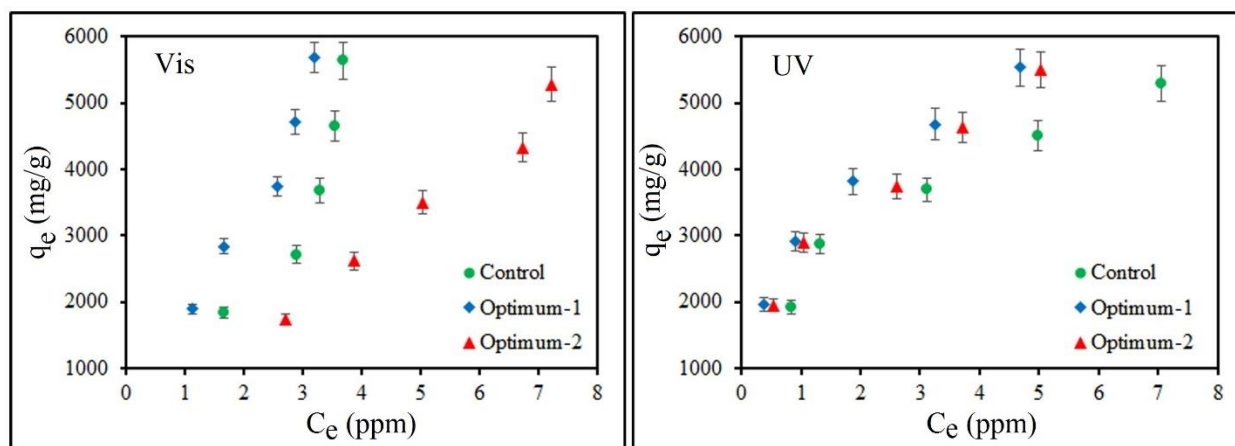
344 In all Eq.s, q_e (mg/g) and C_e (mg/L) are Equilibrium capacity and concentration respectively, in Eq.
345 (12), the absorption capacity constant of Freundlich is K_F (mg/g)(L/g)ⁿ. In Eq. (13), the constant
346 Langmuir capacity K_L (L/mg), maximum monolayer coverage capacities q_m (mg/g). In Eq. (14),
347 the equilibrium constant of Temkin is k_T (J/mol), and the heat absorption Constant is b_1 (g.L⁻¹.K);
348 if b_1 is more than zero, the absorption process would be exothermic [27]. The theoretical saturation
349 capacity q_m (mg/g), $\epsilon = RT \ln(1 + \frac{1}{C_e})$, and D-R isotherm constant β (mol²kJ⁻²) in Eq. (15), in the

350 lateral relation, the global constant of gases R is equivalent to 8.314 and the absolute ambient
351 temperature in terms of Kelvin T . There is a significant constant in the Langmuir relation called
352 the Langmuir intrinsic absorption (R_L) which is determined from Eq. (16). If the intrinsic
353 absorption is more than 1, the absorption capacity is undesirable. When it is 0, the reaction is
354 irreversible. When it is 1 to 0 is absorption is desirable. Langmuir intrinsic absorption depends on

355 the K_L and the initial concentration (C_0). K_L indicates the porosity and active absorption Sites of
 356 an absorbent, so the higher the Langmuir constant, the greater the absorption capacity and can set
 357 the Langmuir intrinsic absorption between 1-0.

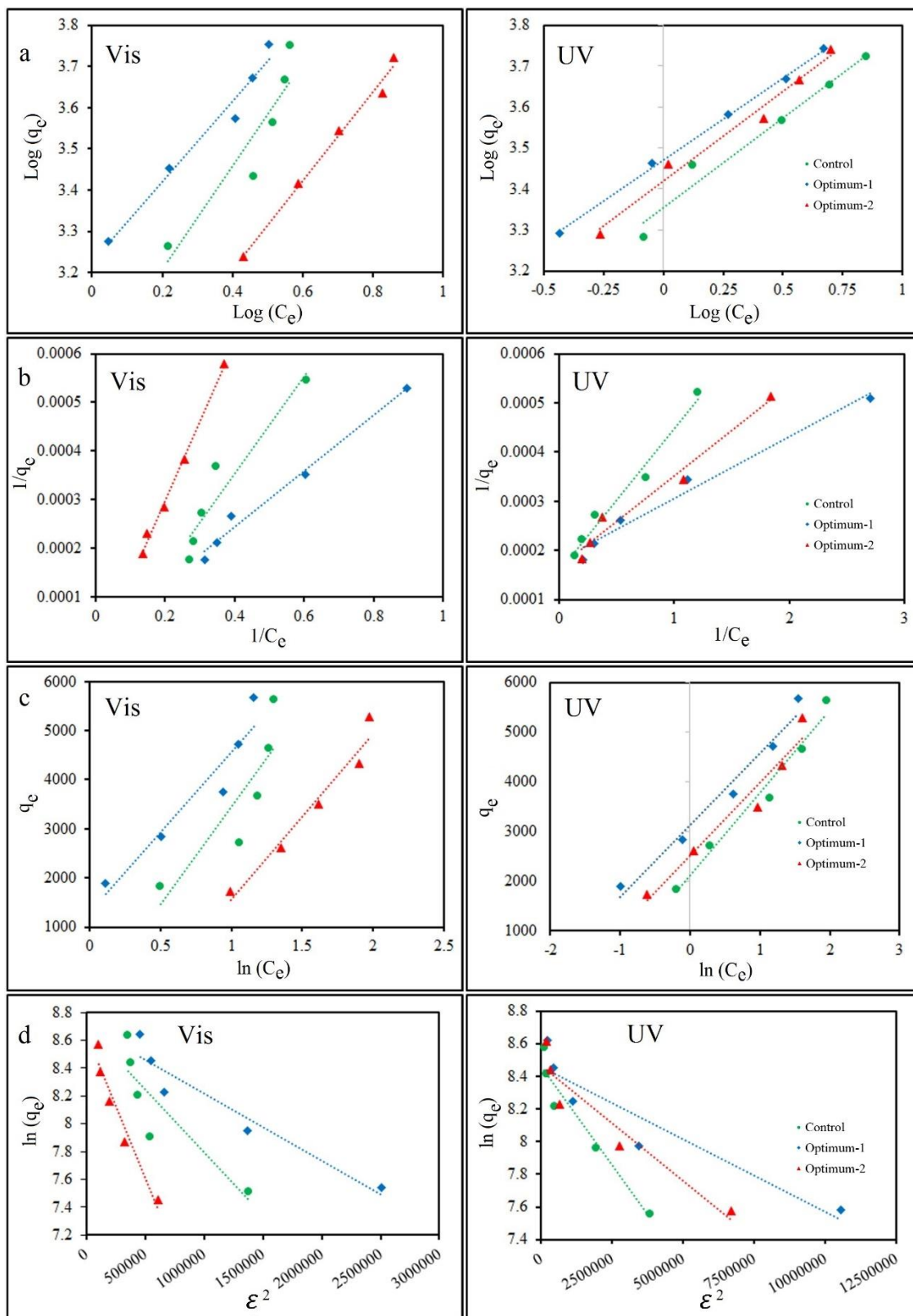
$$358 \quad R_L = \frac{1}{1+k_L C_0} \quad (16)$$

359 In Fig. 10, the Optimum-1 has the highest equilibrium absorption capacity at different
 360 concentrations in both visible light and UV radiation environments; in addition, the Optimum-2
 361 has less absorption capacity in visible light than the control sample, although in the UV chamber
 362 due to the activation of the photocatalytic properties of TiO_2 , its absorption capacity is higher than
 363 the control sample.



364
 365 **Fig. 10.** Absorption isotherms in Vis and UV irradiation

366 From Table 4 and Fig. 11, based on the Freundlich isotherm model (average $R^2=0.94$), the orders
 367 of the functions (n) vary 0.8-1. Langmuir isotherm model indicates that only the optimum-1 K_L
 368 has a positive range, and the intrinsic isotherm absorption $R_L=0.5-0.75$ is in visible light. Other
 369 samples with an R_L of more than one cannot demonstrate desirable absorption at higher
 370 concentrations. k_T (Temkin equilibrium constant) varies from 1.5 to 0.5, and due to the low R^2 for
 371 optimum-1 and control, just can be referred for optimum-2. Average $q_m= 5830$ mg/g of the D-R
 372 model reports that with an average of the correlation coefficient, 0.93 for the optimum-1 and
 373 optimum-2 samples, which is significant with the obtained results. Freundlich was the best model
 374 of isotherm of MB absorption in visible light with χ^2 averages, 89 mg/g.



375
 376 **Fig. 11.** Absorption isotherm models, a) Freundlich, b) Langmuir, c) Temkin, and d) D-R in
 377 visible light and UV chamber for optimum-1 (blue), optimum-2 (red), and control (green)

378 Table 4 and Fig.11 show that the Optimum-1 based on the Freundlich isotherm model has the
 379 highest order of absorption equilibrium capacity (n) equivalent to 2.5. Langmuir model points out
 380 that the equilibrium Langmuir constants (K_L) vary from 0.66 to 2. All optimal and control samples
 381 have intrinsic isotherm absorption (R_L) between 0.008-0.024. The equilibrium constant of the
 382 Optimum-1 is higher than other samples. Finally, the significant result is that the best model of
 383 absorption isotherm is Freundlich (averages of $R^2=0.98$, and $\chi^2=27.5$). According to Table 4,
 384 orders of absorption concentration capacities (n) in visible light are approximately first order,
 385 while the orders (n) in the UV chamber rise to 2.2 to 2.5 order, which indicates the effect of UV
 386 radiation and photocatalytic activity of TiO_2 nanoparticles in the absorption of MB.

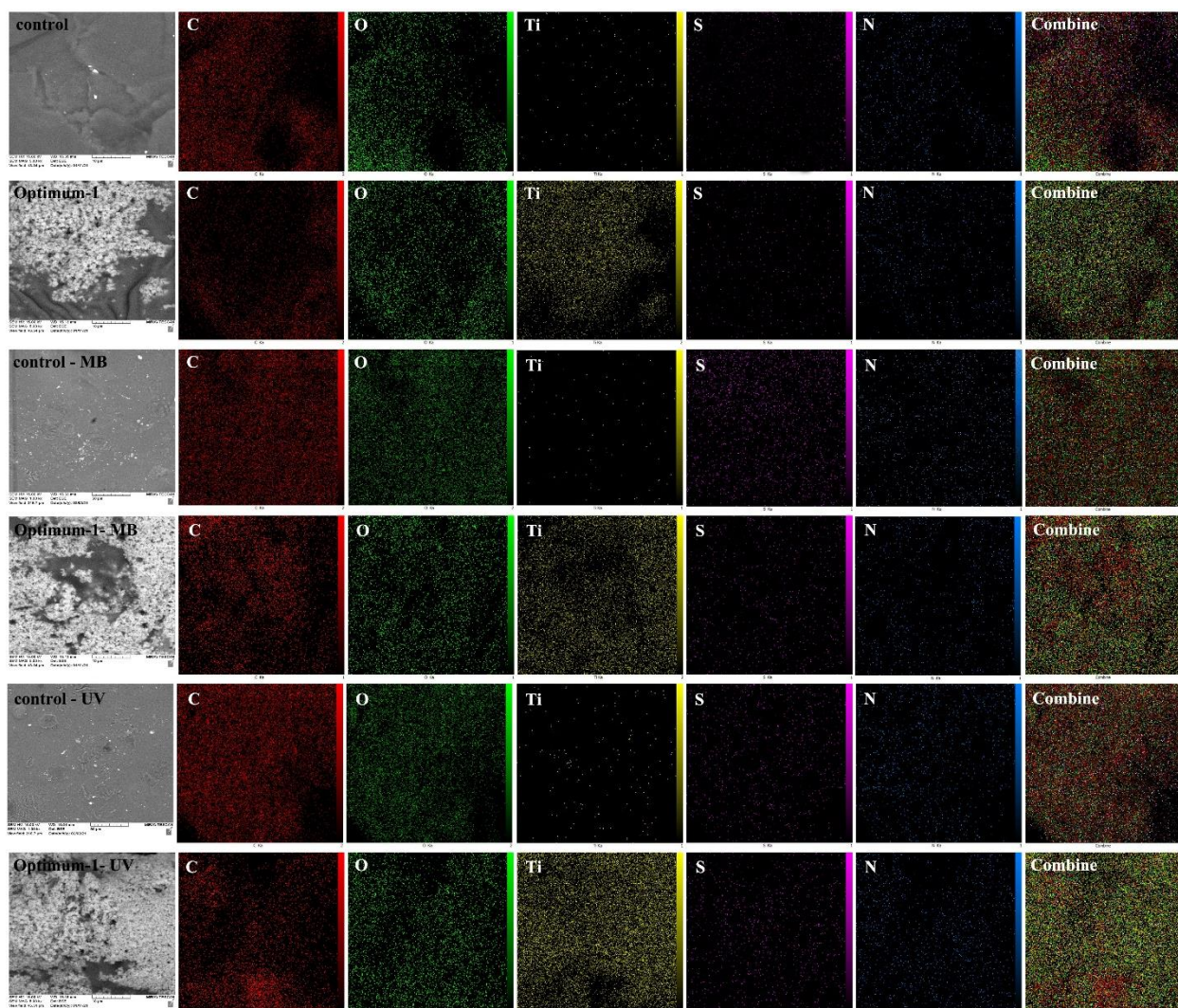
387 **Table 4.** Absorption isotherm models in visible light and UV chamber

constants	Vis			UV		
	Control	Optimum-2	Optimum-1	Control	Optimum-2	Optimum-1
Freundlich model						
K_F	904.48	601.45	1683.06	2626.63	2259.95	2966.19
n	0.796	0.931	1.0236	2.2831	2.277	2.499
R^2	0.8617	0.9885	0.9704	0.969	0.981	0.998
χ^2	216.35	12.73	40.059	126.8	5.78	0.157
Langmuir model						
q_m	-20000	-33333.33	100000	5000	5000	5000
K_L	-0.05	-0.01875	0.0166	0.666	1	2
R^2	0.9085	0.9943	0.9844	0.9786	0.972	0.9769
χ^2	401.1	0.63	80.17	332.95	424.01	227.4
C_0	Langmuir intrinsic absorption (R_L)					
60ppm	NA	1.6	0.750	0.0697	0.0476	0.0243
50ppm	NA	2.285	0.666	0.0476	0.0322	0.0163
40ppm	NA	4	0.600	0.0361	0.0243	0.0123
30ppm	NA	16	0.545	0.0291	0.0196	0.0099
20ppm	NA	NA	0.500	0.0243	0.0163	0.00823
Temkin model						
b_1	3949.2	3358.3	3261.6	2106.4	2509.7	3123.6
k_T	0.8816	0.5877	1.495	2.201	1.798	1.557
R^2	0.7404	0.9561	0.909	0.976	0.953	0.971
χ^2	212.61	36.82	67.40	0.641	77.17	5.787
D-R model						
q_m	6004.7	5656.7	6009.5	4733.87	4741.45	4696.15
β	$9*10^{-7}$	$2*10^{-6}$	$5*10^{-7}$	$2*10^{-7}$	10^{-7}	$9*10^{-8}$
R^2	0.7721	0.946	0.9183	0.939	0.899	0.879
χ^2	372.56	99.42	169.03	66.45	120.84	188.63

388

389 **3.10. EDS Analysis**

390 Image of the fracture surface of the samples before and after MB absorption was carried out to
391 detect existing elements. The elements carbon (red), oxygen (green), nitrogen (blue), sulfur
392 (purple), and titanium (yellow) were assessed in Fig. 12. It is clear that the control samples lack
393 the element titanium.



394
395 **Fig. 12.** Images of element mapping, before and after absorption in both visible and UV
396 irradiation environments

397 Mapping Optimum-1 elements after MB absorption (after immersion in MB solution) in visible
398 light, increasing sulfur, nitrogen, and carbon densities represent that the absorption of MB in
399 Optimum-1. Mapping Optimum-1 elements after MB absorption in UV light, compared to
400 Optimum-1 after absorption in visible light, declining carbon and oxygen justify that degradation

401 of MB appears with the Optimum-1. Radical reactions among oxygen, water, and MB due to the
 402 presence of TiO₂ in UV light; degradation and absorption arise simultaneously. Based on MB
 403 degradation, CO₂ is produced ideally [16]. Finally, the results of this study are compared with
 404 previous works and the results are summarized in Table 5.

405 **Table 5.** Comparison of results with similar studies.

Name of absorber	Type of photocatalyst material	q_{max} (mg/g)	Removal (%)	Swelling (%)	Ref.
Microparticle of Zn(II)-porphyrin/poly(acrylic acid)	Zn(II)-porphyrin	-	80-97	-	[17]
TiO ₂ /poly[acrylamide-co-(acrylic acid)] composites	TiO ₂	-	90	-	[28]
Poly (vinyl alcohol) / poly(acrylic acid) / TiO ₂ / graphene oxide nanocomposite hydrogels	TiO ₂ / graphene oxide	-	20-95	80-200	[29]
poly(acrylic acid)-grafted polyethersulfone / n nitrogen-doped carbon quantum dots-titanium dioxide	n nitrogen-doped carbon quantum dots-titanium dioxide (NCQDs-TiO ₂)	-	94.41	-	[30]
TiO ₂ /guar gum hydrogel composites	TiO ₂	180	20-90	-	[23]
sodium alginate poly (acrylic acid) ZnO hydrogel nanocomposites	ZnO	1300	-	2000	[2]
This work	TiO ₂	1996	95-99	190-600	-

406 Comparison between the results of other studies confirms the effect of acrylic acid hydrogels
 407 containing photocatalytic nanoparticles prepared in this study. For example, Santoso et al. showed
 408 that with increasing the pH of the environment, the rate of absorption and removal of methylene
 409 blue increased [23]. They attributed this effect to creating negative charges in the alkaline
 410 environment on the adsorbent and increasing the adsorption of MB. These results are similar to
 411 the results obtained in our study.

412 **4. Conclusions**

413 The examinations of swelling and absorption of MB in visible light and UV radiation present as
414 three test design responses that fundamentally can be reached the conclusions: The swelling
415 assessment was optimal when the amounts of TiO₂, GG, and BDOD approached the minimum
416 range. The absorption assessment in visible and UV light at the optimal status when pH=8, GG (2
417 wt %), BDOD (2 mol %), and TiO₂ (5-7 mol %). Likewise, MB absorption due to photocatalytic
418 activation of TiO₂ was reported favorably at pH=6 in the UV chamber. SEM, XRD, and FTIR
419 analysis indicated the presence of intensity of nanoparticles in the hydrogel. Superlative
420 equilibrium absorption capacities (q_e) of Optimum-1 were 1934 (mg/g) in visible light and 1996
421 (mg/g) under UV irradiation. The results of equilibrium absorption capacity (q_e) and absorption
422 capacity (q_t) at different times showed that the optimum-1 had the topmost absorption capacity at
423 various minutes (q_t) and concentrations (C_e). The absorption kinetic results for the optimal samples
424 generally showed that the absorption in visible light was pseudo-first-order and under UV radiation
425 trended to be second-order. Significantly, based on the Elovich, the initial absorption rate (α) of
426 MB under UV light was 3-13 times faster than visible light. The results of the Freundlich
427 absorption isotherm model for the Optimum-1 demonstrated that the order of equilibrium
428 concentration (n) in visible light was 1.07 and under UV radiation was 2.49 relative to the
429 equilibrium absorption capacity. Langmuir model results pointed out that the optimum-1 had the
430 higher equilibrium constant (K_L) than the other samples and put the intrinsic absorption (R_L)
431 between 0-1 in the two environments. Ultimately, EDS analysis confirmed the presence of TiO₂
432 nanoparticles, degradation MB to CO₂, and more demanded absorption of MB under UV radiation
433 than visible light.

434 **CRedit authorship contribution statement**

435 **Seyyed Masud Naserzade:** Conceptualization, Investigation, Methodology, Experimental,
436 Formal analysis, Data curation, Results interpretation, Writing – original draft – editing.
437 **Mohsen Shahrousvand:** Conceptualization, Supervision, Experimental, Methodology, Data
438 checking, Writing – review & editing. **Jamshid Mohammadi-Rovshandeh:** Project
439 administration, Supervision, Data checking, Writing – review & editing. **Hojjat Basati:** Data
440 checking, Experimental.

441

442 **Declaration of Competing Interest**

443 The authors declare that they have no known competing financial interests or personal
444 relationships that could have appeared to influence the work reported in this paper.

445 **Appendix A. Supporting information**

446 Supplementary data associated with this article can be found in the online version at doi:XXX.

447 **Uncategorized References**

- 448 [1] C. Chen, H. Chen, X. Guo, S. Guo, G. Yan, Advanced ozone treatment of heavy oil refining
449 wastewater by activated carbon supported iron oxide, *Journal of Industrial and Engineering*
450 *Chemistry*, 20 (2014) 2782-2791.
- 451 [2] E. Makhado, S. Pandey, K.D. Modibane, M. Kang, M.J. Hato, Sequestration of methylene blue
452 dye using sodium alginate poly (acrylic acid)@ ZnO hydrogel nanocomposite: kinetic, isotherm,
453 and thermodynamic investigations, *International Journal of Biological Macromolecules*, 162
454 (2020) 60-73.
- 455 [3] S. Tamjidi, H. Esmaeili, B.K. Moghadas, Application of magnetic adsorbents for removal of
456 heavy metals from wastewater: a review study, *Materials Research Express*, 6 (2019) 102004.
- 457 [4] M.T. Yagub, T.K. Sen, H. Ang, Equilibrium, kinetics, and thermodynamics of methylene blue
458 adsorption by pine tree leaves, *Water, Air, & Soil Pollution*, 223 (2012) 5267-5282.
- 459 [5] N. Daneshvar, M. Hejazi, B. Rangarany, A. Khataee, Photocatalytic degradation of an
460 organophosphorus pesticide phosalone in aqueous suspensions of titanium dioxide, *Journal of*
461 *Environmental Science and Health, Part B*, 39 (2004) 285-296.
- 462 [6] S.M. Doke, G.D. Yadav, Novelities of combustion synthesized titania ultrafiltration membrane
463 in efficient removal of methylene blue dye from aqueous effluent, *Chemosphere*, 117 (2014) 760-
464 765.
- 465 [7] M.H. Dehghani, B. Karimi, M.S. Rajaei, The effect of aeration on advanced coagulation,
466 flotation and advanced oxidation processes for color removal from wastewater, *Journal of*
467 *Molecular Liquids*, 223 (2016) 75-80.
- 468 [8] N. Mohabansi, V. Patil, N. Yenkie, A comparative study on photo degradation of methylene
469 blue dye effluent by advanced oxidation process by using TiO₂/ZnO photo catalyst, *Rasayan*
470 *Journal of Chemistry*, 4 (2011) 814-819.
- 471 [9] J. Wang, H. Chen, Catalytic ozonation for water and wastewater treatment: Recent advances
472 and perspective, *Science of The Total Environment*, 704 (2020) 135249.
- 473 [10] D.T.T. Trinh, W. Khanitchaidecha, T. Threrujirapapong, A. Nakaruk, Effect of Dye and NaCl
474 Concentrations on Methylene Blue Dye Removal by Electrocoagulation.
- 475 [11] Y. Kuang, X. Zhang, S. Zhou, Adsorption of methylene blue in water onto activated carbon
476 by surfactant modification, *Water*, 12 (2020) 587.
- 477 [12] F. Yu, F. Tian, H. Zou, Z. Ye, C. Peng, J. Huang, Y. Zheng, Y. Zhang, Y. Yang, X. Wei,
478 ZnO/biochar nanocomposites via solvent free ball milling for enhanced adsorption and
479 photocatalytic degradation of methylene blue, *Journal of Hazardous Materials*, 415 (2021) 125511.
- 480 [13] S. Tang, Z. Wang, D. Yuan, Y. Zhang, J. Qi, Y. Rao, G. Lu, B. Li, K. Wang, K. Yin, Enhanced
481 photocatalytic performance of BiVO₄ for degradation of methylene blue under LED visible light
482 irradiation assisted by peroxydisulfate, *Int. J. Electrochem. Sci*, 15 (2020) 2470-2480.

483 [14] J. Akhtar, M. Tahir, M. Sagir, H.S. Bamufleh, Improved photocatalytic performance of Gd
484 and Nd co-doped ZnO nanorods for the degradation of methylene blue, *Ceramics International*, 46
485 (2020) 11955-11961.

486 [15] T.A. Kurniawan, Z. Mengting, D. Fu, S.K. Yeap, M.H.D. Othman, R. Avtar, T. Ouyang,
487 Functionalizing TiO₂ with graphene oxide for enhancing photocatalytic degradation of methylene
488 blue (MB) in contaminated wastewater, *Journal of environmental management*, 270 (2020)
489 110871.

490 [16] R. Zuo, G. Du, W. Zhang, L. Liu, Y. Liu, L. Mei, Z. Li, Photocatalytic degradation of
491 methylene blue using TiO₂ impregnated diatomite, *Advances in Materials Science and*
492 *Engineering*, 2014 (2014).

493 [17] H.P. Mota, R.F. Quadrado, B.A. Iglesias, A.R. Fajardo, Enhanced photocatalytic degradation
494 of organic pollutants mediated by Zn (II)-porphyrin/poly (acrylic acid) hybrid microparticles,
495 *Applied Catalysis B: Environmental*, 277 (2020) 119208.

496 [18] S. Yari, J. Mohammadi-Rovshandeh, M. Shahrousvand, Preparation and optimization of
497 Starch/Poly vinyl alcohol/ZnO nanocomposite films applicable for food packaging, *Journal of*
498 *Polymers and the Environment*, (2021) 1-16.

499 [19] A. Behraves, M. Shahrousvand, A. Goudarzi, Poly (acrylic acid)/gum arabic/ZnO semi-IPN
500 hydrogels: synthesis, characterization and their optimizations by response surface methodology,
501 *Iranian Polymer Journal*, 30 (2021) 655-674.

502 [20] S. Zenoozi, G.M.M. Sadeghi, M. Shahrousvand, M. Rafiee, Preparation and optimization of
503 polyurethane/crosslinked poly acrylic acid semi-IPNs containing multi wall carbon nanotube
504 applicable for artificial tendon, *Colloids and Surfaces A: Physicochemical and Engineering*
505 *Aspects*, (2022) 128415.

506 [21] M. Hajikhani, M.M. Khangahi, M. Shahrousvand, J. Mohammadi-Rovshandeh, A. Babaei,
507 S.M.H. Khademi, Intelligent superabsorbents based on a xanthan gum/poly (acrylic acid) semi-
508 interpenetrating polymer network for application in drug delivery systems, *International journal of*
509 *biological macromolecules*, 139 (2019) 509-520.

510 [22] S.M. Hosseini, M. Shahrousvand, S. Shojaei, H.A. Khonakdar, A. Asefnejad, V. Goodarzi,
511 Preparation of superabsorbent eco-friendly semi-interpenetrating network based on cross-linked
512 poly acrylic acid/xanthan gum/graphene oxide (PAA/XG/GO): characterization and dye removal
513 ability, *International journal of biological macromolecules*, 152 (2020) 884-893.

514 [23] S.P. Santoso, A.E. Angkawijaya, V. Bundjaja, C.-W. Hsieh, A.W. Go, M. Yuliana, H.-Y.
515 Hsu, P.L. Tran-Nguyen, F.E. Soetaredjo, S. Ismadji, TiO₂/guar gum hydrogel composite for
516 adsorption and photodegradation of methylene blue, *International Journal of Biological*
517 *Macromolecules*, 193 (2021) 721-733.

518 [24] Y. Huang, H. Yu, C. Xiao, pH-sensitive cationic guar gum/poly (acrylic acid) polyelectrolyte
519 hydrogels: Swelling and in vitro drug release, *Carbohydrate polymers*, 69 (2007) 774-783.

520 [25] J.V. Pasikhani, N. Gilani, A.E. Pirbazari, Improvement the wastewater purification by TiO₂
521 nanotube arrays: The effect of etching-step on the photo-generated charge carriers and
522 photocatalytic activity of anodic TiO₂ nanotubes, *Solid State Sciences*, 84 (2018) 57-74.

523 [26] M. Benjelloun, Y. Miyah, G.A. Evrendilek, F. Zerrouq, S. Lairini, Recent Advances in
524 Adsorption Kinetic Models: Their Application to Dye Types, *Arabian Journal of Chemistry*,
525 (2021) 103031.

526 [27] R. Rossetto, G.M. Maciel, D.G. Bortolini, V.R. Ribeiro, C.W.I. Haminiuk, Acai pulp and
527 seeds as emerging sources of phenolic compounds for enrichment of residual yeasts
528 (*Saccharomyces cerevisiae*) through biosorption process, *LWT*, 128 (2020) 109447.

- 529 [28] W. Kangwansupamonkon, W. Jitbunpot, S. Kiatkamjornwong, Photocatalytic efficiency of
530 TiO₂/poly [acrylamide-co-(acrylic acid)] composite for textile dye degradation, *Polymer*
531 *Degradation and Stability*, 95 (2010) 1894-1902.
- 532 [29] Y.-E. Moon, G. Jung, J. Yun, H.-I. Kim, Poly (vinyl alcohol)/poly (acrylic
533 acid)/TiO₂/graphene oxide nanocomposite hydrogels for pH-sensitive photocatalytic degradation
534 of organic pollutants, *Materials Science and Engineering: B*, 178 (2013) 1097-1103.
- 535 [30] Z.W. Heng, W.C. Chong, Y.L. Pang, C.H. Koo, Self-assembling of NCQDs-TiO₂
536 nanocomposite on poly (acrylic acid)-grafted polyethersulfone membrane for photocatalytic
537 removal and membrane filtration, *Materials Today: Proceedings*, 46 (2021) 1901-1907.

538

Supplementary Files

This is a list of supplementary files associated with this preprint. Click to download.

- [Supportingdata.docx](#)
- [Graphicalabstract.jpg](#)